excited a second time, all within 35 ps. We have estimated the value of $p(2)$ and find it to be less than $8 \times 10^{-4}$ at our maximum intensity.

To directly demonstrate the non-classical sub-poissonian statistics of our source, we measured the intensity correlation function of the emitted light with the coincidence set-up of Fig. 1d. For both the single-molecule (Fig. 4a) and background (Fig. 4b) cases, the histograms show the expected peak pattern, given the time pattern of the photon emission in the inset of Fig. 2. For poissonian light, such as that from an attenuated pulsed laser or the fluorescence from the background excited by the laser pulses, the central peak is identical in intensity and shape to the lateral ones (Fig. 4b). In the case of a single molecule, the central peak should vanish altogether as no more than one single photon can be emitted by the molecule. The ratio of the central peak's area to the area of the lateral peaks is the signature of the sub-poissonian statistics of the light emitted by our source. The residual peak at zero delay in Fig. 4a arises from coincidence events involving background photons excited during each laser pulse. In our experiment, the background signal shows a lifetime of about 4 ns, which indicates that it arises from weak fluorescence from out-of-focus terrylene molecules, not from Raman scattering.

It is convenient to compare the probability distribution $p(m)$ for our source to that expected from a Poisson distribution by means of the Mandel parameter $Q_s = (\sigma^2 - n_{av})/n_{av}$, where $\sigma^2$ is the variance of the distribution and $n_{av}$ is the average number of photons[26]. At the highest pumping power, the probabilities of our source are $p(0) = 0.14$, $p(1) = 0.86$ and $p(m > 1) \approx 0$. This distribution is radically different from that for a pulsed coherent source with the same $n_{av} = 0.86$: $p_{coh}(0) = 0.42$, $p_{coh}(1) = 0.36$, $p_{coh}(2) = 0.16$, .... The Mandel parameter of our source is $Q_s = -0.86$, not far from $-1$, the value expected for a perfect single-photon emitter, and far from 0, the value for a poissonian source. The Mandel parameter $Q_d$ of the detected photon counts is naturally affected by the light detection efficiency[27]. Using $Q_d = Q_s(\eta/2)$, we find $Q_d \approx -3\%$.

The parameters of our source (repetition rate and single-photon generation probability) are limited only by the laser system used; nevertheless, the current performance already surpasses that of previous work. This high performance combined with the simplicity of our source may make it suitable for a variety of quantum optical experiments and for other applications where triggered single photons are needed. Photons are emitted into a range of solid angles, which can limit the detection efficiency; however, optical solutions to this problem can be envisaged, that is, one can imagine that the single molecule could be coupled to a single cavity mode to reduce losses, change the emission pattern, or modify the emission lifetime and thus increase the emission rate. To reduce the background (from out-of-focus molecules or Raman scattering), reduced terrylene doping, pumping with $z$-axis polarized light, or use of a crystalline system with a more favourable orientation of the single absorber can be utilized. With further development, single molecules in solids may soon provide compact and reliable sources of single photons. □

Received 27 January; accepted 15 August 2000.


1. Meystre, P. & Sargent, M. III *Elements of Quantum Optics* (Springer, Berlin, 1991).
2. Drummond, P. D. *Quantum Squeezing* (Springer, Berlin, 1999).
3. Special issue on quantum information. *Phys. World* **11**(3), (1998).
4. Bennett, C. H., Brassard, G. & Ekert, A. K. Quantum cryptography. *Sci. Am.* **267**(4), 50–57 (1992).
5. Turchette, Q. A., Hood, C. J., Lange, W., Mabuchi, H. & Kimble, H. J. Measurement of conditional phase shifts for quantum logic. *Phys. Rev. Lett.* **75,** 4710–4713 (1995).
6. Parkins, A. S., Marte, P., Zoller, P., Carnal, O. & Kimble, H. J. Quantum-state mapping between multilevel atoms and cavity light fields. *Phys. Rev. A* **51,** 1578–1596 (1995).
7. Cirac, J. I., Zoller, P., Kimble, H. J. & Mabuchi, H. Quantum state transfer and entanglement distribution among distant nodes in a quantum network. *Phys. Rev. Lett.* **78,** 3221–3224 (1997).
8. Kuhn, A., Hennrich, M., Bondo, T. & Rempe, G. Controlled generation of single photons from a strongly coupled atom-cavity system. *Appl. Phys. B* **69,** 373–377 (1999).
9. Imamoglu, A., Schmidt, H., Woods, G. & Deutsch, M. Strongly interacting photons in a nonlinear cavity. *Phys. Rev. Lett.* **79,** 1467–1470 (1997).
10. Imamoglu, A. & Yamamoto, Y. Turnstile device for heralded single photons: coulomb blockade of electron and hole tunneling in quantum confined p-i-n heterojunctions. *Phys. Rev. Lett.* **72,** 210–213 (1994).
11. Kim, J., Benson, O., Kan, H. & Yamamoto, Y. A Single-photon turnstile device. *Nature* **397,** 500–503 (1999).
12. Brunel, C., Lounis, B., Tamarat, P. & Orrit, M. Triggered source of single photons based on controlled single molecule fluorescence. *Phys. Rev. Lett.* **83,** 2722–2725 (1999).
13. Xie, X. S. & Trautman, J. K. Optical studies of single molecules at room temperature. *Annu. Rev. Phys. Chem.* **49,** 441–480 (1998).
14. Moerner, W. E. & Orrit, M. Illuminating single molecules in condensed matter. *Science* **283,** 1670–1676 (1999).
15. Ambrose, W. P., Goodwin, P. M., Martin, J. C. & Keller, R. A. Single-molecule detection and photochemistry on a surface using near-field optical-excitation. *Phys. Rev. Lett.* **72,** 160–163 (1994).
16. Ambrose, W. P. *et al.* Fluorescence photon antibunching from single molecules on a surface. *Chem. Phys. Lett.* **269,** 365–370 (1997).
17. De Martini, F., Di Giuseppe, G. & Marrocco, M. *Phys. Rev. Lett.* **76,** 900–903 (1996).
18. Kiston, S. C., Jonsson, P., Rarity, J. G. & Tapster, P. R. Intensity fluctuation spectroscopy of small numbers of dye molecules in a microcavity. *Phys. Rev. A* **58,** 620–627 (1998).
19. Fleury, L., Sick, B., Zumofen, G., Hecht, B. & Wild, U. P. High photo-stability of single molecules in an organic crystal at room temperature observed by scanning confocal optical microscopy. *Mol. Phys.* **95,** 1333–1338 (1998).
20. Kulzer, F., Koberling, F., Christ, T., Mews, A. & Basche, T. Terrylene in p-terphenyl: single molecule experiments at room temperature. *Chem. Phys.* **247,** 23–34 (1999).
21. Basché, T., Moerner, W. E., Orrit, M. & Talon, H. Photon antibunching in the fluorescence of a single dye molecule trapped in a solid. *Phys. Rev. Lett.* **69,** 1516–1519 (1992).
22. Fleury, L., Segura, J.-M., Zumofen, G., Hecht, B. & Wild, U. P. Nonclassical photon statistics in single molecule fluorescence at room temperature. *Phys. Rev. Lett.* **84,** 1148–1151 (2000).
23. Kummer, S., Basché, T. & Bräuchle, C. Terrylene in p-terphenyl: a novel single crystalline system for single molecule spectroscopy at low temperatures. *Chem. Phys. Lett.* **229,** 309–316 (1994).
24. Plakhotnik, T., Moerner, W. E., Palm, V. & Wild, U. P. Single molecule spectroscopy: maximum emission rate and saturation intensity. *Opt. Commun.* **114,** 83–88 (1995).
25. Buttler, W. T. *et al.* Quantum key distribution over 1 km. *Phys. Rev. Lett.* **81,** 3283–3286 (1998).
26. Short, H. & Mandel, L. Observation of sub-poissonian photon statistics. *Phys. Rev. Lett.* **51,** 384–387 (1983).
27. Mandel, L. Sub-poissonian photon statistics in resonance fluorescence. *Opt. Lett.* **4,** 205–207 (1979).
28. Miller, G. D. *et al.* 42%-efficient single-pass cw second-harmonic generation in periodically poled lithium niobate. *Opt. Lett.* **22,** 1834–1836 (1997).



### Acknowledgements

We thank Lightwave Electronics for use of the mode-locked Nd-YAG laser, M. Fejer and M. Fayer for providing non-linear crystals, and the Stanford Synchrotron Radiation Laboratory for providing the pulse height analyser. B. L. thanks D. Wright for assistance and NATO for Fellowship support.


Correspondence and requests for materials should be addressed to W.E.M. (e-mail: moerner@stanford.edu).

# Logical computation using algorithmic self-assembly of DNA triple-crossover molecules

**Chengde Mao*, Thomas H. LaBean†, John H. Reif† & Nadrian C. Seeman ***

** Department of Chemistry, New York University, New York, 10003, USA & †Department of Computer Science, Duke University, Durham, North Carolina 27707, USA*

**Recent work[1–3] has demonstrated the self-assembly of designed periodic two-dimensional arrays composed of DNA tiles, in which the intermolecular contacts are directed by 'sticky' ends. In a mathematical context, aperiodic mosaics may be formed by the self-assembly of 'Wang' tiles[4], a process that emulates the operation of a Turing machine. Macroscopic self-assembly has been used to perform computations[5]; there is also a logical equivalence between DNA sticky ends and Wang tile edges[6,7]. This suggests that the self-assembly of DNA-based tiles could be used to perform DNA-based computation[8]. Algorithmic aperiodic self-assembly requires greater fidelity than periodic self-assembly,**

**because correct tiles must compete with partially correct tiles. Here we report a one-dimensional algorithmic self-assembly of DNA triple-crossover molecules[9] that can be used to execute four steps of a logical (cumulative XOR) operation on a string of binary bits.**

A variety of different DNA tile types have been used in previous assemblies, including double-crossover molecules[1], triple-crossover molecules[9], and parallelograms produced from Holliday junction analogues[3]. Here we have used triple-crossover molecules; their molecular structure is illustrated in Fig. 1a. The molecule contains four strands (shown in red, green, blue and purple) that self-assemble through Watson–Crick base pairing to produce three double helices in a roughly planar arrangement; each double helix is connected to adjacent double helical domains at two points where their strands cross over between them. The ends of the central double helix are closed by hairpin loops, but the other helices can terminate in sticky ends containing information that directs the assembly of the tiles.

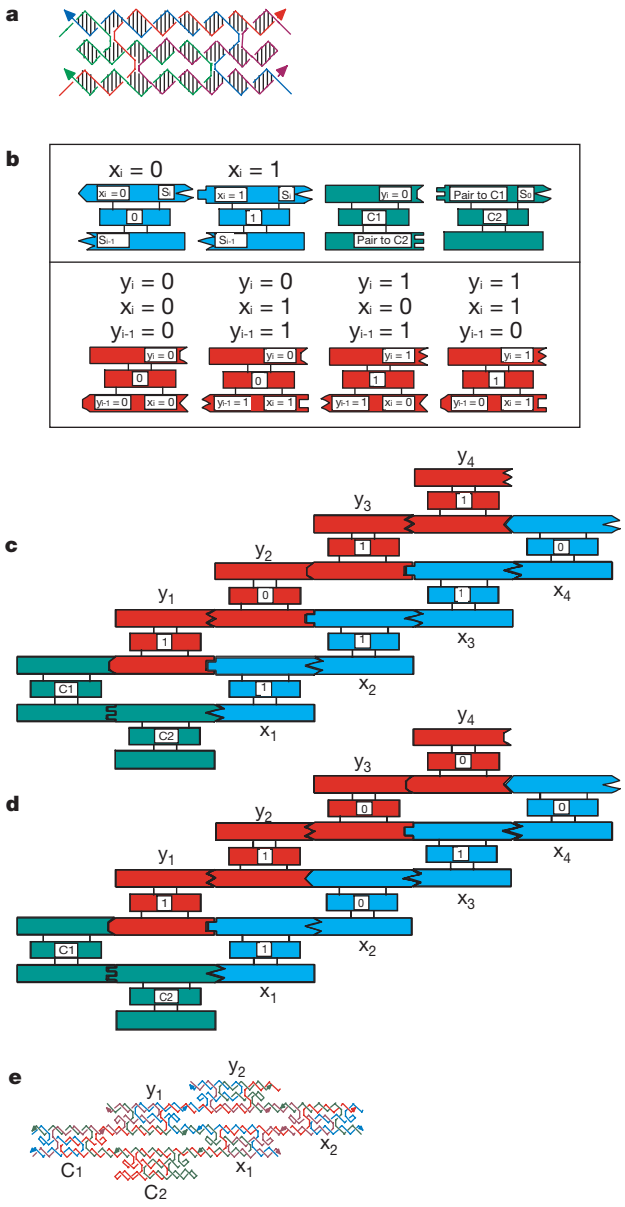


**Figure 1** Calculation of cumulative XOR by self-assembly of DNA tiles. **a**, An individual triple-crossover tile. The four coloured backbone strands assemble to form three double-helical domains; arrowheads indicate 3′ ends. **b**, Component tiles. The three helical domains are drawn as rectangles, flanked by sticky ends shown as geometrical shapes. The value of each tile is in the central rectangle. The meaning of each sticky end is also indicated. Shown are the two x tiles (blue), the four y tiles (red), and the initialization corner tiles, C1 and C2 (green). The $y_i$ tiles are upside down from the $x_i$ tiles. **c**, **d**, The two calculations performed. The values of each tile are the same as in **b**, and the sticky ends are the same, although the labels have been omitted for clarity. The tiles are shown assembled to perform the cumulative XOR calculation; note the complementarity of sticky-ended association at each molecular interface. All sticky ends are asymmetric, so that when the same meanings touch (for example, $x_i = 0$ pairing with $x_i = 0$), the sequences are complementary, but not self-complementary. The operations are designed to proceed from lower left to upper right, because the $x_i$ and C1 and C2 tiles have longer sticky ends than the $y_i$ tiles. After the first y tile has been added, $x_1 = 1$ and $y_1 = 1$, for both arrays, because $y_1 = x_1$. In the next step, the array in **c** contains $x_2 = 1$: because $x_2 = y_1$, $y_2$ should be 0, and only the y tile with value 0 and inputs $y_{i-1}$ and $x_i = 1$ fits properly between $y_1$ and $x_2$. In **d**, $x_2 = 0$, so $x_2 \neq y_1$, and $y_2$ should be 1, as shown. The sequences are available in the Supplementary Information. **e**, The reporter strand. At the end of the assembly, the reporter strand running through the x diagonal array, around the corner, and then back up the y diagonal array is ligated, thereby associating the calculated output with the input. The strand structure in the vicinity of the corner is shown, and the reporter strand is drawn with a thick red line.

In periodic assemblies, the sticky ends contain positional information that directs the associations of one or more tile types to produce a periodic lattice. Here, the sticky ends serve the same role, but the self-assembly of the tiles is used to perform a computation, and the arrangement of the tiles does not display simple periodicity. Figure 1b shows the tiles used to perform the cumulative XOR calculation. The tiles are represented schematically; the three helices are depicted as connected rectangular forms terminating in sticky ends, which are represented as geometrical shapes, or non-cohesive blunt ends and hairpins, which are drawn flush.

The result of the XOR operation is a 0 if two input numbers are the same (two zeros or two ones), but it is 1 if one of the two numbers is 0 and the other is 1. The cumulative XOR consists of a series of Boolean inputs $x_1$, $x_2$, $x_3$, ... $x_n$, and the output is also a series of Booleans, $y_1$, $y_2$, $y_3$, ... $y_n$, where $y_1 = x_1$, and for $i > 1$, $y_i = y_{i-1}\mathrm{XOR}x_i$. The value of any $y_i$ in these calculations also reports the even or odd parity of the first $i$ values of $x$. Thus, two different kinds of input x tiles are needed, one whose value is 0 and a second whose value is 1. Chemically, the value of a tile, 0 or 1, is denoted by the presence of a restriction site: Pvu II (CAGCTG) represents 0 and EcoR V (GATATC) represents 1.

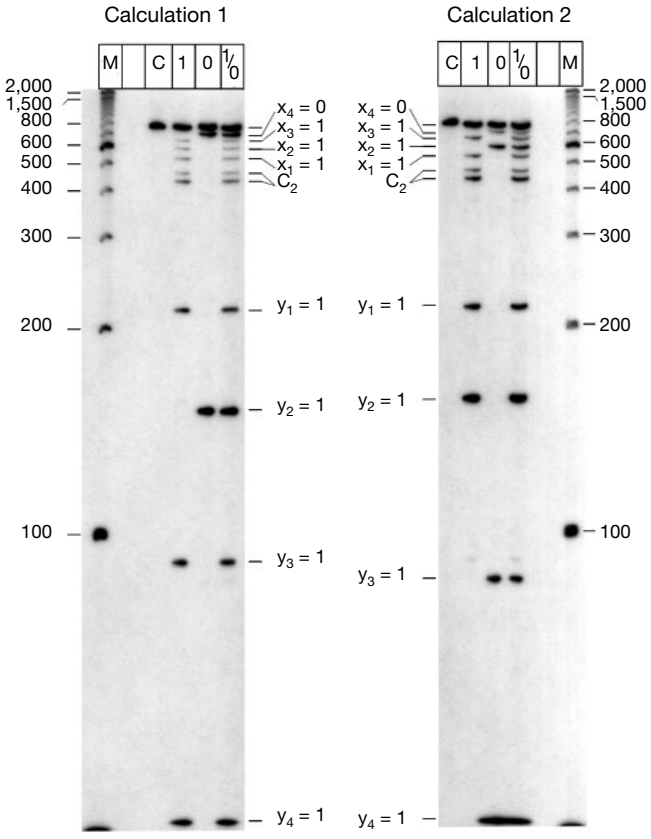


**Figure 2** Denaturing gels illustrating cumulative XOR calculations. Two 6% denaturing gels are shown, corresponding to the two calculations described. M, lanes containing 100-mer marker ladders; C, lanes containing undigested reporter strands. The lanes digested with Pvu II are labelled 0, to indicate that sensitivity to this enzyme represents a tile with the value zero, and those digested with EcoR V are labelled 1, because the site for that enzyme represents a value of one. A lane combining the two individual digestions is labelled 1/0. The bands corresponding to the input values $x_4$, $x_3$, $x_2$ and $x_1$ are visible at the tops of the lanes, in descending order. The C2 tile contains a hairpin with an EcoR V site, so the site is present twice in the reporter strand at that location. The bands corresponding to the output values $y_1$, $y_2$, $y_3$ and $y_4$ are visible at the bottom of the gel. Faint bands corresponding to erroneous Pvu II cleavage are visible near $y_2$ in calculation 1 and $y_3$ in calculation 2. A faint band corresponding to erroneous EcoR V cleavage is present near $y_3$ in calculation 1.

The x tiles are shown in blue in Fig. 1b: Their value (0 or 1) is shown in their central rectangle, the upper-left sticky end reports this value, and the upper-right and lower-left sticky ends provide the means of connecting successive x tiles. These sticky ends are shown as geometrically complementary, as they would be for a general set of 16 parallel calculations. However, to demonstrate the efficacy of the procedure, the calculations performed here are definite four-bit calculations for which the order of the input x tiles was specified exactly by a series of different sticky ends.

Like x tiles, two values of y tiles are necessary, again representing 0 and 1. However, there are two ways to get each of these results: the value of a y tile can be 0 either because both inputs are 0 or because both are 1; likewise, the value of a y tile can be 1 because the value of one input is 0 and the other is 1, or vice versa. Thus, four different y tiles are needed.

The y tiles are shown in red in Fig. 1b. The tile values again are displayed on the central domain, and this value is reported by the sticky end on the right of the upper domain. The two inputs derive from the sticky ends on the left ($y_{i-1}$) and right ($x_i$) of the bottom domain. We note that the same sticky end in the input domain represents a given input, independent of the other end. For example, the right-side sticky end $x_i = 1$ has the same shape (sticky end) regardless of whether the left-side sticky end represents $y_{i-1} = 0$ (leading to a tile value of 1) or $y_{i-1} = 1$ (leading to a tile value of 0). There are only two different left sticky ends in the input (bottom) domain, and likewise only two different right sticky ends. Consequently, both sticky ends on each tile must pair correctly for the proper $y_i$ tile to be inserted in the assembly. In contrast to periodic assembly, where correct tiles compete with incorrect tiles for each site in the lattice, here correct tiles are competing with partially correct tiles.

We have performed two different XOR-related self-assemblies, illustrated in Fig. 1c and d. In addition to the x and y tiles, two corner tiles, C1 and C2 (green in Fig. 1b) are used to initialize the two values of $x_1$ and $y_1$, and to connect the input to the output. The self-assembly in Fig. 1c has the inputs $x_1 = x_2 = x_3 = 1$ and $x_4 = 0$. These correspond to output values of $y_1 = 1$, $y_2 = 0$, and $y_3 = y_4 = 1$. In a second self-assembly (Fig. 1d), $x_1 = 1$, $x_2 = 0$, $x_3 = 1$ and $x_4 = 0$, corresponding to $y_1 = y_2 = 1$ and $y_3 = y_4 = 0$. Note that for $i > 1$, the sticky ends on the bottom domain of each $y_i$ tile complement those on the $y_{i-1}$ tile on its left and the $x_i$ tile on its right.

Once the self-assembly has occurred, it is necessary to extract the answer. For this purpose, each molecular tile contains a 'reporter strand'[10], which traverses the tile in a diagonal pathway[9]; the reporter strand is illustrated as a thick red strand in the tile shown in Fig. 1a, which is an x-type tile. Following self-assembly, the reporter strands are ligated to each other to produce a long reporter strand that contains the inputs and outputs of the calculation. The ligated long reporter strand in the vicinity of the corner of the assembly is shown as a thick red strand on the molecular diagram in Fig. 1e.

The sticky ends used in the assembly of the $C_1$–$C_2$–$x_1$–$x_2$–$x_3$–$x_4$ unit contain seven nucleotides, and the sticky ends used to include the $y_i$ tiles in the assembly contain five nucleotides. The tiles were first assembled individually from their component strands by cooling slowly from 90 °C to room temperature, as done previously[1–3]. 20-μl aliquots of stock solutions (in USB ligation buffer) of both C tiles (100 nM), the four x tiles (100 nM), and the four y tiles (400 nM) were then combined and incubated for 30 min each at temperatures of 37, then 22, and finally 4 °C. During incubation and subsequent steps, 20-μl aliquots of three double helices, each with a sticky end (one helix to pair with the free sticky end on $x_4$ and two helices to pair with the two possible free sticky ends on $y_4$), that contained radioactively labelled PCR primers (800 nM) were also present in solution.

Ligation was initiated by adding 20 units of T4 DNA ligase and,

over a 3-hour period, the solution was brought slowly to 16 °C as ligation proceeded. The strand was amplified by polymerase chain reaction (PCR), using the primers that were ligated to each end of the long reporter strand. A strand of the proper length was eluted from a denaturing gel, was re-annealed, and was subjected to restriction by either of the restriction enzymes. The results are displayed in Fig. 2. The answer produces a barcode display, much like that used in ref. 11 to visualize the answers to RNA computation of chess problems. The correct answers are evident as dark bands in the gels shown in Fig. 2.

Small proportions of incorrect bands are visible on the original gels for both calculations. Thus, in lane 1 (EcoR V) of calculation 1, there is an incorrect band at the 0 position of $y_2$, and a similar incorrect band in the 0 lane at $y_3$ is also present. However, if the array fills from the corner, some of the incorrect $y_3$ intensity could result from 'correct' molecules propagating the previous error. Similarly, calculation 2 has one detectable error band resulting from cleavage of EcoR V at $y_3$.

We estimate the error level to be about 2–5%, but quantitative error analysis is complicated by differential cleavage activities between the two enzymes, combined with the possibility of star-activity (sequence infidelity) and probable multiple cleavage of the same strand. Also, the individual enzymes cleave with different activities at different sites, as seen in the differential cleavage of the two EcoR V sites in the C2 tile. We may have reduced our observation of self-assembly errors by selecting only those tiles that ligated correctly, because the enzyme specificity for exact pairing, although imperfect[12], may have performed some discrimination for the system. A previous two-molecule, single-step competition experiment estimated error rates below 1.6% (ref. 13).

The algorithmic molecular assembly described here demonstrates a non-trivial DNA computation done by self-assembly. Examples of SAT (satisfaction) problems solved in a DNA context[11,14,15] entailed laboratory operations for each clause in a logical statement, whereas a single self-assembly step is used here. This suggests that computation by self-assembly may be scalable. Another recent work[16] also uses only a single assembly step, but its scalability relies on proper hairpin formation in very long single-stranded molecules.

XOR computation on pairs of bits (as done here) can be used for executing a one-time pad cryptosystem that provides theoretically unbreakable security[17]. Other applications could involve the algorithmically directed self-assembly of intricate patterns and smart materials. We used y tiles repetitively in both assemblies, and would need no more species of y tiles, regardless of the length of the calculation. Thus, if the assembly principles applied here can be extended to two and three dimensions, it will be possible to prepare nanoscale patterns and smart materials by laying out components algorithmically, without the need to specify and prepare a unique element for every position of the array.

By using more nucleotides in the sticky ends of the input tiles than the output tiles, we have used the principle of 'frames'[6,7,18] This feature performs the computation in the presence of a well-defined border. Such borders are likely to be useful, because they set limits on the extent of the calculation or patterning; combining framed arrays will facilitate a modular approach to the process. □

Received 27 April; accepted 3 August 2000.


1. Winfree, E., Liu, F., Wenzler, L. A. & Seeman, N. C. Design and self-assembly of two-dimensional DNA crystals. *Nature* **394,** 539–544 (1998).
2. Liu, F., Sha, R. & Seeman, N. C. Modifying the surface features of two-dimensional DNA crystals. *J. Am. Chem. Soc.* **121,** 917–922 (1999).
3. Mao, C., Sun, W. & Seeman N. C. Designed two-dimensional DNA Holliday junction arrays visualized by atomic force microscopy. *J. Am. Chem. Soc.* **121,** 5437–5443 (1999).
4. Wang, H. in *Proceedings of a Symposium in the Mathematical Theory of Automata* 23–26 (Polytechnic Press, New York, 1963).
5. Rothemund, P. W. K. Using lateral capillary forces to compute by self-assembly. *Proc. Nat. Acad. Sci. USA* **97,** 984–989 (2000).
6. Winfree, E. in *DNA Based Computers: Proceedings of a DIMACS Workshop, April 4, 1995, Princeton University* (eds Lipton, R. J. & Baum, E. B.) 199–221 (American Mathematical Society, Providence, RI, 1996).
7. Winfree, E. *Algorithmic Self-Assembly of DNA*. PhD Thesis, Caltech (1998).
8. Adleman, L. Molecular computation of solutions to combinatorial problems. *Science* **266,** 1021–1024 (1994).
9. LaBean, T. *et al.* The construction, analysis, ligation and self-assembly of DNA triple crossover complexes. *J. Am. Chem. Soc.* **122,** 1848–1860 (2000).
10. Seeman, N. C. Nucleic acid nanostructures and topology. *Angew. Chem. Int. Edn Engl.* **37,** 3220–3238 (1998).
11. Faulhammer, D., Cukras, A. R., Lipton, R. J. & Landweber, L. F. Molecular computation: RNA solutions to chess problems. *Proc. Natl Acad. Sci. USA* **97,** 1385–1389 (2000).
12. Harada, K. & Orgel, L. E. Unexpected substrate specificity of T4 DNA ligase revealed by *in vitro* selection. *Nucleic Acids Res.* **21,** 2287–2291 (1993).
13. Winfree, E., Yang, X. & Seeman, N. C. in *DNA Based Computers: II Proceedings of a DIMACS Workshop, June 10–12, 1996, Princeton University* (eds Landweber, L. F. & Baum, E. B.) 217–254 (American Mathematical Society, Providence, RI, 1999).
14. Liu, Q. *et al.* DNA computing on surfaces. *Nature* **403,** 175–179 (2000).
15. Pirrung, M. C. *et al.* The arrayed primer extension method for DNA microchip analysis. Molecular computation of satisfaction problems. *J. Am. Chem. Soc.* **122,** 1873–1882 (2000).
16. Sakamoto, K. *et al.* Molecular computation by DNA hairpin formation. *Science* **288,** 1223–1226 (2000).
17. Gehani, A., LaBean, T. H. & Reif, J. H. in *DNA Based Computers: Proceedings of a DIMACS Workshop, June 1999, MIT* (ed. E. Winfree) (DIMACS Series in Discrete Mathematics and Theoretical Computer Science, American Mathematical Society, Providence, RI, in the press).
18. Reif, J. H. in *DNA Based Computers: III Proceedings of a DIMACS Workshop, June 23–25, 1997, University of Pennsylvania* (eds Rubin, H. & Wood D. H.) 217–254 (American Mathematical Society, Providence, RI, 1999).


**Supplementary information** is available on *Nature*'s World-Wide Web site (http://www.nature.com) or as paper copy from the London editorial office of *Nature*.


### Acknowledgements

We thank E. Winfree and A. Carbone for valuable discussions. This work has been supported by grants from DARPA and the National Science Foundation to J.H.R. and N.C.S.; ONR, USAF, NSF and NIH grants to N.C.S.; and NSF and ARO grants to J.H.R.


Correspondence and requests for materials should be addressed to N.C.S. (e-mail: ned.seeman@nyu.edu).

# Nano-sized transition-metal oxides as negative-electrode materials for lithium-ion batteries

**P. Poizot, S. Laruelle, S. Grugeon, L. Dupont & J-M. Tarascon**

*Laboratoire de Réactivité et Chimie des Solides, Université de Picardie Jules Verne, CNRS UPRES A 6007, 33 rue Saint Leu, F-80039, Amiens, France*

**Rechargeable solid-state batteries have long been considered an attractive power source for a wide variety of applications, and in particular, lithium-ion batteries are emerging as the technology of choice for portable electronics. One of the main challenges in the design of these batteries is to ensure that the electrodes maintain their integrity over many discharge–recharge cycles. Although promising electrode systems have recently been proposed[1–7], their lifespans are limited by Li-alloying agglomeration[8] or the growth of passivation layers[9], which prevent the fully reversible insertion of Li ions into the negative electrodes. Here we report that electrodes made of nanoparticles of transition-metal oxides (MO, where M is Co, Ni, Cu or Fe) demonstrate electrochemical capacities of 700 mA h $g^{-1}$, with 100% capacity retention for up to 100 cycles and high recharging rates. The mechanism of Li reactivity differs from the classical Li insertion/deinsertion or Li-alloying processes, and involves the formation and decomposition of $Li_2O$, accompanying the reduction and oxidation of metal nanoparticles (in the range 1–5 nanometres) respectively. We expect that the use of transition-metal nanoparticles to enhance surface electrochemical reactivity will lead to further improvements in the performance of lithium-ion batteries.**